Robotica (2015) volume 33, pp. 848–864. © Cambridge University Press 2014
doi:10.1017/S0263574714000587

Hand-eye servo and impedance control for manipulator arm to capture target satellite safely

Gan Ma†,‡, Zhihong Jiang†,‡*, Hui Li†,‡, Junyao Gao†,‡, Zhangguo Yu†,‡, Xuechao Chen†,‡, Yun-Hui Liu†,§ and Qiang Huang†,‡,¶

†*The Intelligent Robotics Institute, School of Mechatronical Engineering, Beijing Institute of Technology, Beijing, P. R. China*
‡*Key Laboratory of Biomimetic Robots and Systems, Ministry of Education, Beijing, P. R. China*
§*The Department of Mechanical and Automation Engineering, The Chinese University of Hong Kong, Sha Tin, N.T., Hong Kong*
¶*Key Laboratory of Intelligent Control and Decision of Complex System, Beijing, P. R. China*

(Accepted February 13, 2014. First published online: March 17, 2014)

SUMMARY
A crucial problem is the risk that a manipulator arm would be damaged by twisting or bending during and after contacting a target satellite. This paper presents a solution to minimize the risk of damage to the arm and thereby enhance contact performance. First, a hand-eye servo controller is proposed as a method for accurately tracking and capturing a target satellite. Next, a motion planning strategy is employed to obtain the best-fit contacting moments. Also, an impedance control law is implemented to increase protection during operation and to ensure more accurate compliance. Finally, to overcome the challenge of verifying algorithms for a space manipulator while on the ground, a novel experimental system with a 6-DOF (degree of freedom) manipulator on a chaser field robot is presented and implemented to capture a target field robot; the proposed methods are then validated using the experimental platform.

KEYWORDS: Hand-eye servo; Impedance control; Safe; Satellite capture; Space robot.

1. Introduction

Robotic systems are expected to play an increasingly significant role in future on-orbit services such as refueling, repairing, and re-orbiting. One application of great importance is the autonomous capture of a target spacecraft using a manipulator arm. This particular application is the key task in missions involving deep space exploration, on-orbit charging, on-orbit module replacement, and on-orbit maintenance.

Orbital Express has previously demonstrated the technology used for the autonomous capture of a target satellite. *Orbital Express* is a space mission managed by *the United States Defense Advanced Research Projects Agency* (DARPA).[1] The goal of the *Orbital Express Space Operations Architecture Program* is to validate the technical feasibility of robotic applications, autonomous on-orbit refueling, and reconfiguration of satellites to support a broad range of future US national security and commercial space programs.[2] In addition to *Orbital Express*, other countries have also dedicated resources to the development of space robotics, such as *ETS-VII*[3] and *Canadarm2*.[4]

The capturing process can be divided into three main phases: the pre-contact phase (following and tracing the target satellite); the contact phase (capturing the target satellite); and the post-contact phase (maintaining contact with the target satellite and stabilizing the system). In the pre-contact phase, the main objective is to accurately trace and quickly capture the target. A failure to do this may result in adverse performance during the contact phase and post-contact phase. Also, it may

* Corresponding author. E-mail: jiangzhihong@bit.edu.cn

reduce the ability of the controller to maintain stable system operations. If unstable operation occurs, the manipulator arm may become bended or twisted and even damaged when the chaser and target satellites come into contact. Therefore, in order to enhance protection for the manipulator arm, the entire operation must be configured for optimal performance.

Various methods have been proposed to accurately follow and trace a target satellite in space during the pre-contact phase using camera-generated information. Nagamatsu *et al.*[5] proposed a capture strategy for the retrieval of a skew-whiff satellite using a space manipulator arm. Xu *et al.*[6] developed a capture method for non-cooperative targets in space. Xu and Liang[7] also developed a trajectory planning method for a free-floating robot. Kobayashi and Tsuda[8] studied the coplanar motion between a space robot and its target; however, the control of the space robot was suboptimal.

Unexpected movement may occur between a target satellite and a manipulator arm during the contact phase and post-contact phase due to contact force and other disturbances in space. The safe and successful capture of a target satellite requires that the manipulator arm move in compliance with the target satellite. A significant amount of research has been dedicated to this situation. Gu and Xu[9] employed an adaptive control method to control the under-actuated non-linear dynamics of space robotic systems. Wang and Xie[10] proposed a recursive adaptive algorithm for free-floating manipulators. Dimitrov *et al.*[11] used a conservation of momentum method to suppress the relative motion between two satellites, thereby simultaneously dealing with the two satellites. Wei *et al.*[12] introduced a “dynamic grasping area" to describe the collision process and to establish a grasping area control equation. Yoshida *et al.*[13] also presented a method to maintain contact with the target satellite during capture using a ground-based experiment system that used two industrial robots.

The above-mentioned methods provide a theory for the autonomous capture of a target satellite. However, these research have not adequately addressed the protection of the manipulator arm when capturing a target satellite. This paper examined the protection of the manipulator arm as follows. First, a high-precision, high-speed, image-based visual servo algorithm for a hand-eye camera system was used to ensure accurate capture. Second, an autonomous on-line path planning method for a space manipulator that combined the two vision systems was used to ensure accurate capture. A strategy to choose the best-fit times for the insertion of the manipulator arm into the target satellite was developed. Third, due to the uncertain contact force between the manipulator arm and the moving target satellite during the contact phase and post-contact phase, an impedance control was employed to protect the manipulator arm from bending and twisting. Finally, a ground experiment platform consisting of a manipulator and a moving target was used to verify the proposed method.

2. Space Robotic System Modeling

2.1. Free-floating manipulator model

This section addresses the modeling of a space free-floating manipulator system. In a free-floating system, the spacecraft is permitted to freely translate and rotate in response to manipulator motions. In this case, both the movement of the target and manipulator must be described in a common reference frame: the inertial frame.

The Virtual Manipulator Approach[14] was proposed to describe the kinematics and dynamics of a free-floating space manipulator system. The kinematics and dynamics of a manipulator, spacecraft, and payload are easily described in terms of the Virtual Manipulator. Umetani and Yoshida[15] presented the Generalized Jacobian Matrix to model a free-floating manipulator system, which was successfully applied to revolved motion rate control and resolved acceleration control of a free-floating space manipulator.[15,16]

In this section, the Lagrangian method is used to model the space robotic system. Figure 1 shows the free-floating manipulator model, consisting of a base and n rigid links. The chaser satellite is simplified to a rigid base with mass m_0. The manipulator arm is attached to the rigid mass. A force/torque sensor is fixed at the tip of the manipulator to sense contact forces and torques. The satellite on the right is the target satellite and is modeled as a floating rigid body of mass m_t.

The origin of the base frame (Σ_b) is fixed at the mass center of the base. The end-effector frame (Σ_e) is fixed at the tip of the manipulator. The target frame (Σ_t) is fixed at the left side of the target satellite; and Σ_I is the inertia frame.

https://doi.org/10.1017/S0263574714000587 Published online by Cambridge University Press

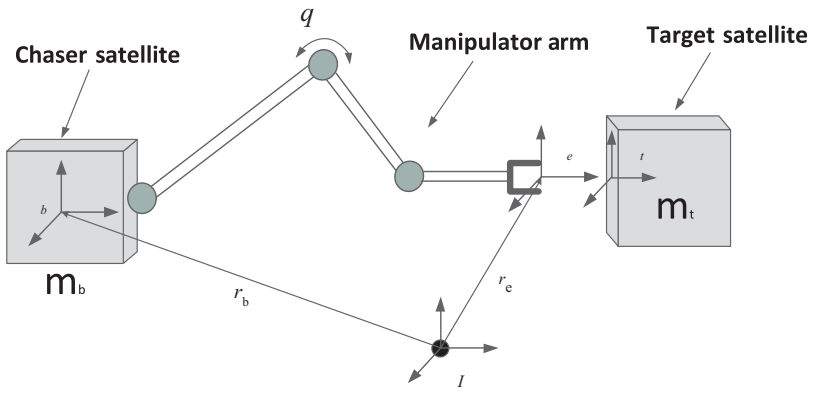

Fig. 1. The free-floating model.

2.2. *Kinematic modeling of the system*

The differential kinematic equation is

$$\begin{bmatrix} v_e \\ \omega_e \end{bmatrix} = J_b \begin{bmatrix} v_0 \\ \omega_0 \end{bmatrix} + J_m \dot{q}, \tag{1}$$

where $J_b \in R^{6\times n}$ is the Jacobian matrix for the base; $J_m \in R^{6\times n}$ is the Jacobian matrix for the arm; v_e is the linear velocity of the end-effector; ω_e is the angular velocity of the end-effector; v_0 is the linear velocity of the base; ω_0 is the angular velocity of the base; and $q \in R^n$ is the joint angle of the manipulator. The total momentum of the space robot is

$$\begin{bmatrix} P_0 \\ L_0 \end{bmatrix} = H_b \begin{bmatrix} v_0 \\ \omega_0 \end{bmatrix} + H_{bm} \dot{q}, \tag{2}$$

where $H_b \in R^{6\times 6}$ is the inertia matrix of the base; $H_{bm} \in R^{6\times n}$ is the coupling inertia matrix of the base and manipulator; P_0 and L_0 are the linear and angular momentum of the system, respectively. Substituting (2) into (1) provides

$$\begin{bmatrix} v_e \\ \omega_e \end{bmatrix} = \left(J_m - J_b H_b^{-1} H_{bm}\right) \dot{q} + J_b H_b^{-1} \begin{bmatrix} P_0 \\ L_0 \end{bmatrix}. \tag{3}$$

For normalization, the kinematic relationship between the operational and the joint space is

$$\dot{x}_e = \left(J_m - J_b H_b^{-1} H_{bm}\right) \dot{q} + \dot{x}_{ge}, \tag{4}$$

where $\dot{x_e} = (v_e^T, \omega_e^T)^T$, $\dot{x}_{ge} \in R^6$ is the velocity of the gravity center of the entire system projected on the end-effector velocity, defined as:

$$\dot{x}_{ge} = J_b H_b^{-1} \begin{bmatrix} P_0 \\ L_0 \end{bmatrix}. \tag{5}$$

2.3. *Dynamic modeling of the system*

Everything is free-floating in a space environment; hence, the dynamic behavior of mechanical links is distinct from ground-based systems. According to rigid body dynamics,[17] the dynamic equations of a free-floating robot with a manipulator arm are

$$\begin{bmatrix} F_b \\ \tau \end{bmatrix} = \begin{bmatrix} H_b & H_{bm} \\ H_{bm}^T & H_m \end{bmatrix} \begin{bmatrix} \ddot{x}_b \\ \ddot{q} \end{bmatrix} + \begin{bmatrix} c_b \\ c_m \end{bmatrix} - \begin{bmatrix} J_b^T \\ J_m^T \end{bmatrix} F_e, \tag{6}$$

https://doi.org/10.1017/S0263574714000587 Published online by Cambridge University Press

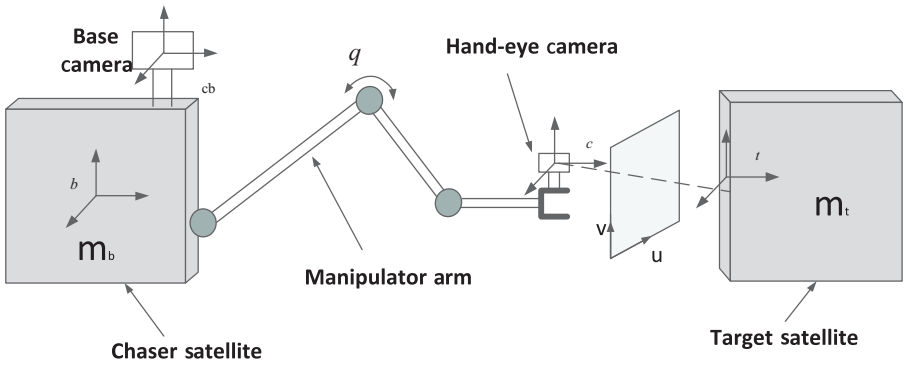

Fig. 2. Vision system structure.

where $H_m \in R^{n\times n}$ is an inertia matrix of the manipulator arm; $c_b \in R^6$ is a velocity dependent non-linear term for the base; $c_m \in R^6$ is a velocity dependent non-linear term for the manipulator; $F_b \in R^6$ is an external force and moment in time on the gravity center of the base; $F_e \in R^6$ is an external force and moment in time on the tip of the manipulator; $\tau \in R^6$ is the joint torque of the manipulator; and $x_b \in R^6$ is the position of the base. If external forces only act on the tip of the manipulator, the equation of motion in the joint space is obtained from (6) and can be written as

$$\tau = H_m^*\ddot{q} - J_m^{*T}F_e + c_m^*, \tag{7}$$

where, for a space robot, $H_m^* \in R^{6\times 6}$ is the generalized inertia matrix; $c_m^* \in R^{6\times 1}$ are the generalized Coriolis and centrifugal forces; and $J_m^* \in R^{6\times n}$ is the generalized Jacobian:[13,16]

$$\begin{cases} H_m^* = H_m - H_{bm}^T H_b^{-1} H_{bm} \\ c_m^* = c_m - H_{bm}^T H_b^{-1} c_b \\ J_m^* = J_m - J_b (H_b^{-1})^T H_{bm} \end{cases}. \tag{8}$$

3. Visual Servoing Control

It is essential to employ a hand-eye visual tracking system to capture the on-line position and attitude of the target because the target satellite arbitrarily moves during the pre-contact phase. This section deals primarily with the visual servoing control algorithm.

Visual servo, also known as Vision-Based Robot Control, is a technique that uses feedback information extracted from a vision sensor to control the motion of a robot. Visual servoing schemes are generally classified into position-based visual servo (PBVS) and image-based visual servo (IBVS).[18] In the PBVS approach,[19,20] the controller is designed using the relative three-dimensional (3D) pose between the camera and the target object, which is estimated from the visual features. However, this approach is sensitive to camera calibration and needs *a priori* 3D model of the target object for the 3D reconstruction. Meanwhile, the controller in the IBVS approach[21,23] is directly designed using the visual features, eliminating the need for 3D reconstruction. Consequently, IBVS is better than PBVS for handling modeling errors and external disturbances.

This paper proposes a high-precision, high-speed, image-based visual servo algorithm for a hand-eye camera system to control the space manipulator. Figure 2 shows the overall structure of the space vision system. There are two stereo cameras on the chaser satellite that capture real-time information about the arrangement of the feature points. One is a base camera that is mounted on the base of the chaser satellite; the other is a hand-eye camera that is mounted on the tip of the manipulator arm. Σ_{cb} is the base camera frame and Σ_c is the hand-eye camera frame. This paper assumed that N ($N >= 3$) feature points were mounted on the target and that the coordinates of the feature points were already known with respect to Σ_t. This section only presents the algorithm of the hand-eye camera system.

https://doi.org/10.1017/S0263574714000587 Published online by Cambridge University Press

3.1. Pinhole model

In this section, the perspective projection method is employed to model the camera projection. Here, the hand-eye camera is a pinhole camera with perspective projection. The two-dimensional (2D) image frame is denoted by $\{u, v\}$. Under this model,

$$y = \frac{1}{z} P\, {}^{c}x_t, \tag{9}$$

where ${}^{c}x_t$ is the homogeneous coordinates of the feature point with respect to the camera frame; z is the depth of the feature points; $y = [u, v]^T$ is the projection coordinate of the feature points on the image plane; and P is the matrix, consisting of the first two rows of the 3×4 perspective projection matrix (M) whose components depend on the intrinsic and extrinsic parameters of the camera:

$$M = \begin{bmatrix} \alpha r_1^T - \alpha \cot\theta r_2^T + u_0 r_3^T & \alpha p_x - \alpha \cot\theta p_y + u_0 p_z \\ \dfrac{\gamma}{\sin\theta} r_2^T + v_0 r_3^T & \dfrac{\gamma}{\sin\theta} p_y + v_0 p_z \\ r_3^T & p_z \end{bmatrix}, \tag{10}$$

where α and γ are the scalar factors of the u and v axes of the image plane, respectively; θ is the angle between the two axes; (u_0, v_0) is the position of the principle point of the camera; r_i^T is the ith row vector of the rotation matrix; and (p_x, p_y, p_z) are the coordinates of the translation vector p.

The relationship between the image-plane velocity of a feature point and the velocity of the point with respect to the camera frame can be described by the image Jacobian matrix; the relationship is

$$\dot{y} = J_{\text{image}} \begin{bmatrix} {}^{c}v_t \\ {}^{c}w_t \end{bmatrix}, \tag{11}$$

where $[{}^{c}v_t, {}^{c}\omega_t]^T$ is the velocity of the feature point with respect to the camera frame, and J_{image} denotes the image Jacobian matrix of the camera, defined as

$$J_{\text{image}} = \begin{bmatrix} \dfrac{\lambda}{z} & 0 & -\dfrac{u}{z} & -\dfrac{uv}{\lambda} & \dfrac{\lambda^2 + u^2}{\lambda} & -v \\ 0 & \dfrac{\lambda}{z} & -\dfrac{v}{z} & \dfrac{-\lambda^2 - v^2}{\lambda} & \dfrac{uv}{\lambda} & u \end{bmatrix}, \tag{12}$$

when N feature points are used; the extended image Jacobian is

$$J_{\text{images}} = \begin{bmatrix} J_{\text{image1}} \\ \cdot \\ \cdot \\ J_{\text{image}N} \end{bmatrix}. \tag{13}$$

3.2. Visual servo controller

This section discusses an algorithm for an accurate visual servo controller that can be used to successfully control the manipulator arm insertion into the target satellite. The design is based on an adaptive controller that utilizes a fixed camera for image-based dynamic control of a robot manipulator.[24] A crucial part of the visual servoing control strategy is to establish a hand-eye visual system for the precise capture of a target satellite. As such, an image-based dynamic visual servo controller is used to track the target satellite. The control objective is to lock the projection of the feature point at a desired constant fixed position (y_{d}) on the image plane.

The desired velocity and acceleration values are both zero, based on the hypothesis that the desired position on the image plane (y_{d}) is constant. This gives the nominal reference:

$$\dot{y}_{\text{r}} = \dot{y}_{\text{d}} - \lambda \Delta y = -\lambda \Delta y, \tag{14}$$

https://doi.org/10.1017/S0263574714000587 Published online by Cambridge University Press

where λ is a positive scalar and Δy is a 2×1 image error vector of the feature point. The velocity estimations of the target compared to the camera frame are deduced from (11):

$$\begin{bmatrix} {}^c\hat{v}_t \\ {}^c\hat{\omega}_t \end{bmatrix} = K \hat{J}^{-1}_{\text{images}} \dot{y}_r, \tag{15}$$

where K is the gain matrix; $\hat{J}^{-1}_{\text{images}}$ is the inverse matrix of the estimation of J_{images}; and the desired target velocities in the camera frame are denoted as $[{}^c v_{td},\ {}^c\omega_{td}]^T$. In order to reach the desired target velocities, the estimation error of the end-effector of the manipulator is denoted by $[\Delta v_e,\ \Delta\omega_e]^T$, where

$$\begin{bmatrix} \Delta v_e \\ \Delta\omega_e \end{bmatrix} = \begin{bmatrix} {}^c\hat{v}_t \\ {}^c\hat{\omega}_t \end{bmatrix} - \begin{bmatrix} {}^c v_{td} \\ {}^c\omega_{td} \end{bmatrix}. \tag{16}$$

Here, the total velocity of the end-effector of the manipulator is denoted by $[v_e,\ \omega_e]^T$, such that

$$\begin{bmatrix} v_e \\ \omega_e \end{bmatrix} = \begin{bmatrix} v_{ed} \\ \omega_{ed} \end{bmatrix} + \begin{bmatrix} \Delta v_e \\ \Delta\omega_e \end{bmatrix}, \tag{17}$$

where $[v_{ed},\ \omega_{ed}]^T$ is the desired velocity of the end-effector which will be discussed in Section 4. Substituting (17) into (1) provides

$$\hat{\dot{q}} = J_m^{-1} \begin{bmatrix} v_{ed} \\ \omega_{ed} \end{bmatrix} + J_m^{-1} \begin{bmatrix} \Delta v_e \\ \Delta\omega_e \end{bmatrix} - J_m^{-1} J_b \begin{bmatrix} v_0 \\ \omega_0 \end{bmatrix}. \tag{18}$$

Based on differentiating Eq. (18), the controller is defined as follows:

$$\tau = H_m^* \hat{\ddot{q}} - J_m^{*T} F_e + c_m^*. \tag{19}$$

4. Autonomous Motion Planner

This section deals with the autonomous planning method of a space manipulator when guided by two stereo cameras. Path planning is an important issue for space robots. Major achievements on this subject were collected by ref. [25] and also recently reviewed in ref. [26].

This paper proposes a method to combine the information of two visual systems in order to ensure accurate capture as well as a best-fit moment concept for the insertion of the manipulator. The pre-contact phase is divided into three sub-phases: the approximate approach phase, which is guided by the base camera; and the adjustment phase and the pre-insertion phase, which are both guided by the hand-eye camera. The main steps are as follows:

1. *Initialization*: initialize the camera parameters to define the actual initial position and attitude of the end-effector (X_{e0}) and of the initial manipulator joint angle (q_0).

2. *Approximate approach phase*: extract image features with the base camera and then guide the manipulator arm close to the target satellite.

3. *Adjustment phase*: when the manipulator arm nears the object ($z < z_{\min}$), then the hand-eye camera takes control. In this phase, the desired end-effector of the manipulator is assumed to be moving at a constant velocity, so the depth of the hand-eye camera is:

$$z = z_{\min} - |v_{ed}|t, \tag{20}$$

where t is the time elapsed since the adjustment phase. Combining (20) with (9) provides the desired ${}^c x_t$ throughout this phase. The differential of the desired ${}^c x_t$ is the desired target velocity $[{}^c v_{td},\ {}^c\omega_{td}]^T$. In this phase, the proposed visual servo algorithm in the previous Section 3 was employed to guide the manipulator to the target.

https://doi.org/10.1017/S0263574714000587 Published online by Cambridge University Press

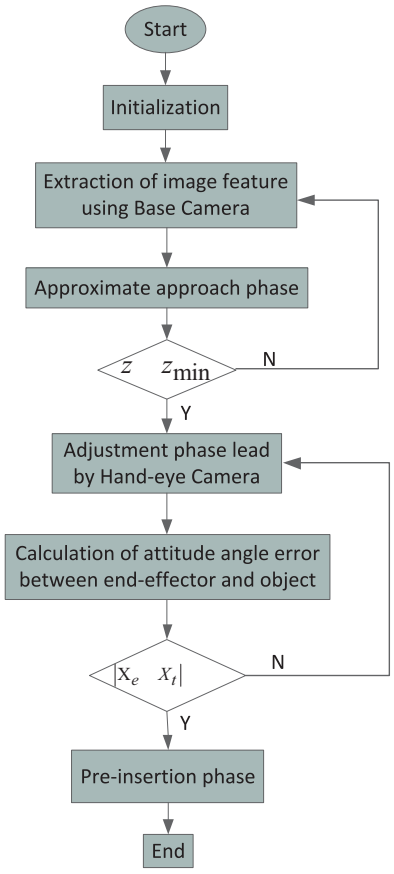

Fig. 3. Flowchart of the autonomous path planning.

4. *Pre-insertion phase*: the best-fit moment for insertion of the manipulator into the target satellite occurs when the manipulator arm is close to the target and the end-effector attitude of the manipulator approximates that of the target (21):

$$|X_{\mathrm{e}} - X_{\mathrm{t}}| <= \varepsilon, \tag{21}$$

where $X_{\mathrm{e}} \in R^{6\times 1}$ is the position and attitude of the front end of the manipulator arm; $X_{\mathrm{t}} \in R^{6\times 1}$ is the position and attitude of the target object; and $\varepsilon \in R^{6\times 1}$ represents the allowable capture error of the position and attitude.

5. *End*: the pre-contact phase is completed after the manipulator arm has arrived at the boundary of the target satellite. This initiates the contact phase and post-contact phase, which are discussed in Section 5. Figure 3 shows the overall procedure.

5. Impedance Control Based Capture

This section addresses the contact phase and the post-contact phase. There is a risk that the contact force may push the target and the robot away from each other because the target satellite arbitrarily moves during the contact phase. In order to capture the target satellite, the contact must be maintained between the end-effector of the manipulator and the target until the capture is finished. Also, unsustainable forces occur at the end-effector due to the uncertainty of the target inertial properties during the contact phase.

In order to solve the above-mentioned problems while protecting the manipulator arm, this study adopts a method[27] that assumes a virtual mass-spring-damper in the end-effector of the manipulator arm. The impedance control law is then employed to maintain compliance of the manipulator arm, thereby maintaining contact with the target satellite while suppressing the relative motion between the arm and satellite.

https://doi.org/10.1017/S0263574714000587 Published online by Cambridge University Press

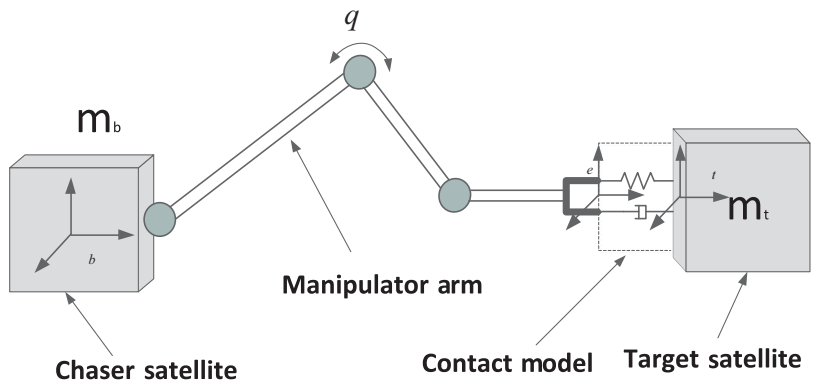

Fig. 4. Satellite contact model.

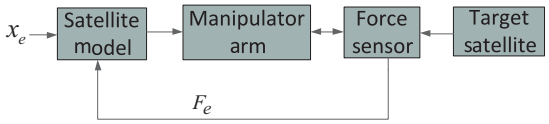

Fig. 5. Control block diagram of the model.

5.1. Contact model

Figure 4 shows a virtual mass-spring-damper in the end-effector of the manipulator arm during contact with the target satellite. In the contact phase, the manipulator arm should be gradually inserted into the target, while maintaining contact with the moving target. In the post-contact phase, the relative movement between the two satellites should be suppressed.

5.2. Impedance control of a space robot

Hogan[28] noted that the central philosophy of impedance control is that the manipulator control system should not just be designed to track motion trajectory, but also to regulate the mechanical impedance of the manipulator. Here, the relationship between the measured interaction effort (F_e) and the motion of the end-effector reference trajectory of the manipulator ($\mathbf{x}_e$) is

$$M\ddot{x}_e + D\Delta\dot{x}_e + K\Delta x_e = F_e, \tag{22}$$

where $F_e \in R^{6\times1}$ is the vector of forces and torques on the manipulator due to contact; Δx_e is the displacement of the end-effector position from the reference point; and $M \in R^{6\times6}$, $D \in R^{6\times6}$, and $K \in R^{6\times6}$ are the desired inertia, damping, and stiffness values, respectively. Substituting the differential of $\dot{x}_e$ according to (4) into (22) gives

$$J^*\ddot{q} = M^{-1}\{F_e - D\Delta\dot{x}_e - K\Delta x_e\} - \dot{J}^*\dot{q} - \ddot{x}_{ge}. \tag{23}$$

Finally, the joint torque, based on impedance control, is theoretically obtained by substituting (23) into (7):

$$\begin{aligned}\tau =& H^*J^{*-1}\{M^{-1}(F_e - D\Delta\dot{x}_e - K\Delta x_e)\\ &- \dot{J}^*\dot{q} - \ddot{x}_{ge}\} - J^{*T}F_e + c^*\end{aligned}. \tag{24}$$

In summary, with proper selection of the constant matrices and the input of the torque (τ) in the joints, the end effector of the manipulator can behave like a mass-damper-spring system. Figure 5 shows the overall structure of the control method.

https://doi.org/10.1017/S0263574714000587 Published online by Cambridge University Press

Table I. Dynamic parameters for the robot.

	Mass (kg)	I_{xx} (kgm^2)	I_{yy} (kgm^2)	I_{zz} (kgm^2)
The upper arm	3.807	0.004865	0.001686	0.005318
The lower arm	2.515	0.002401	0.001043	0.002732
Hand	1.078	0.001673	0.001656	0.002087

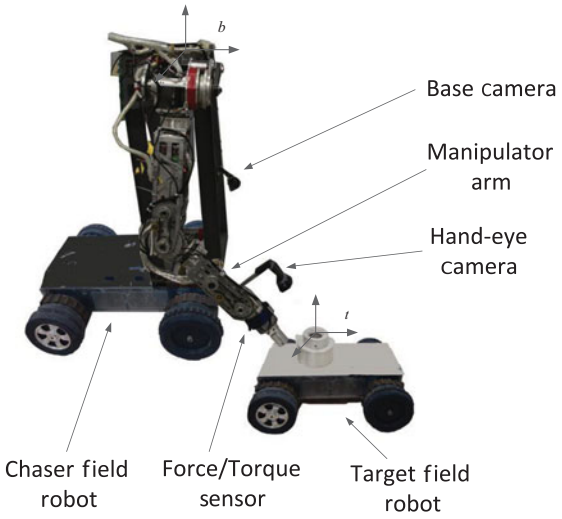

Fig. 6. Experiment platform.

6. Experimental Verification

6.1. Experimental platform

In order to verify the effectiveness of the proposed method, an experimental system was established (Fig. 6). This setup was very similar to the task of *Orbital Express*. Also, in order to simulate a microgravity environment, the gravity compensation factor was considered when designing the platform. Thus, the platform was designed to have enough energy to verify the proposed method and also to provide energy for gravity compensation.

The experimental system was composed of a 6-DOF (degree of freedom) manipulator arm fixed onto a chaser field robot and a target field robot. The field robots simulated the chaser and target satellites. A lightweight manipulator, which simulated a space manipulator, was employed to capture the target field robot. The length of the manipulator was 710 mm and the weight was approximately 7.4 kg. A probe with a cylinder end-tip was attached to the chaser. A six-axis force/torque sensor was mounted on the end-effector and used to detect the forces and torques caused by the environment. The maximum contact force of the manipulator was approximately 100 N. The base frame (Σ_b) was fixed at the shoulder of the manipulator; the target frame (Σ_t) was fixed at the center of the target satellite. Table I shows the dynamic parameters of the platform.

The manipulator arm was divided into three parts: the upper arm, with a length of 330 mm; the lower arm, with a length of 220 mm; and the end-effector, with a length of 160 mm. There were 6 DOFs, designed as follows: 3 DOFs in the shoulder, 2 DOFs in the elbow, and 1 DOF in the wrist. The size of the chaser field robot was 300 × 200 × 200 mm; the weight was approximately 8.432 kg. The size of the chaser field robot was 200 × 150 × 130 mm; the weight was approximately 5.357 kg. The field robot consisted of four omnidirectional wheels, two driving wheels at the front and two passive wheels at the rear.

Figure 6 shows the two stereo cameras mounted on the manipulator. One was located at the base of the manipulator and was used for coarse navigation. The other, a hand-eye camera, was mounted close to the tip of the manipulator. The stereo cameras used SVS cameras, with a sampling rate of 15 fps. The size of the original image was 320 × 240 pixels. The proposed control methods were

https://doi.org/10.1017/S0263574714000587 Published online by Cambridge University Press

employed to capture the moving object by controlling the manipulator arm using the force/torque signals and information from the camera.

Two computers were used in the robot system for visual servoing control and real-time force control. The main control computer (RT-Linux operating system) was responsible for visual servoing control, trajectory planning, force control, and sending the real-time trajectory data to the robot joint driver. The vision computer was used to process the images of the two cameras. It was also used to output the measurement results of the target position and attitude for the camera relative to the main control computer through CAN (controller area network) communication at 1 Mbps. A Maxon DC (direct current) motor with a harmonic reduction driver actuated each robot joint. The DC motors were driven by PWM servo drivers (with a switch frequency of up to 150 kHz).

6.2. Gravity compensation

Different methods have been proposed to simulate a micro-gravity environment while on the ground. Some of these methods include the air-bearing table,[29] ranger neutral buoyancy,[30] fall-falling motion,[31] and the suspension system.[32] Although these methods can effectively verify the algorithm for a space robot, it is difficult to implement these methods in experiments.

The experiment platform, which used a manipulator arm in a chaser field robot to capture a target field robot, could simulate the 2D motion of a space capture experiment. Therefore, it could reasonably validate the effectiveness of the proposed method.

The microgravity environment was validated on ground using a gravity compensation method. In this study, gravity compensation was realized using the model based method[33] because the manipulator was lightweight. Here, the gravity wrench at the base of the manipulator was

$$M_{\mathrm{gc}} = \sum_{1}^{n} \{{}^{b}r_i\} \times \{{}^{b}g\}(m_i), \tag{25}$$

where m_i was the mass of link i; ${}^{b}g$ was the gravitational force vector transformed to the manipulator base coordinate frame; and ${}^{b}r_i$ was the position vector of the ith links center of mass in the manipulator base coordinate frame. The gravity compensation of every joint was obtained by combining M_{gc} with the configuration of the manipulator.

Hence, the proposed method and the gravity compensation method were used to control the platform in order to simulate a space-based capture experiment.

6.3. Experiments on visual based capture

In order to verify the proposed visual servoing control method and the planner, the first experiment moved the manipulator arm close to the moving target under the guide of hand-eye camera. A nozzle cone was assumed as the target. The initial arm joint angles were taken as

$$q_0 = [-20^\circ, 0^\circ, 0^\circ, -55^\circ, 0^\circ, 15^\circ]. \tag{26}$$

The position and attitude of the base and the end-effector were:

$$X_{\mathrm{b}} = [0, 0, 0, 0^\circ, 0^\circ, 0^\circ] \tag{27}$$

and

$$X_{\mathrm{e0}} = [0, 0.1267, -0.5854, 50^\circ, 0^\circ, 0^\circ]. \tag{28}$$

The initial position and attitude of the target were

$$X_{\mathrm{t0}} = [-0.01, 0.2237, -0.5477, -2.67^\circ, 3.58^\circ, -2.13^\circ]. \tag{29}$$

In this experiment, the target was moving at constant velocities at all times:

$$\begin{cases} v_{\mathrm{t}} = [10 \text{ mm/s}, 10 \text{ mm/s}, 0 \text{ mm/s}] \\ \omega_{\mathrm{t}} = [0 \text{ deg/s}, 0 \text{ deg/s}, 0 \text{ deg/s}] \end{cases}. \tag{30}$$

https://doi.org/10.1017/S0263574714000587 Published online by Cambridge University Press

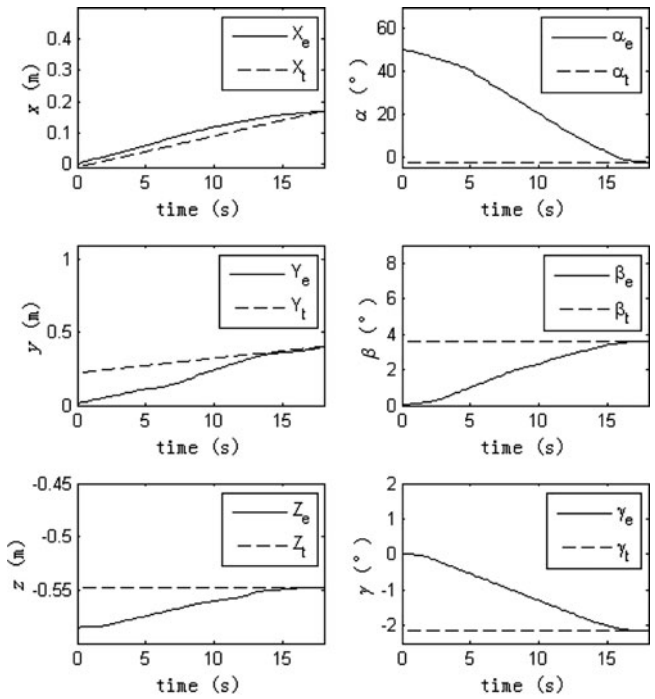

Fig. 7. The variation of the position and attitude of the end-effector and the target.

In order to capture the moving target, the chaser field robot adjusted its attitude and velocity in accordance with the base camera. Simultaneously, the manipulator adjusted its position and attitude under the guide of the hand-eye camera. This experiment only focused on the movement of the manipulator that was under the guide of the hand-eye camera. Figure 7 shows the variation of the position and attitude of the end-effector and the target. Figure 8 shows the relative 3D position and attitude between the end-effector and the target. Figure 9 shows the joint angles of the manipulator arm.

Figures 7 and 8 show that the end-effector of the manipulator closed in on the moving target and also that the attitude of the end-effector approached that of the target. Hence, the proposed visual based planning method performed well for target capture.

6.4. Experiments on force controlled capture

After the manipulator arm arrived at the boundary of the target robot, the contact model came into effect. The contact between the end-effector of the manipulator and the target must be maintained until the capture was completed and the two objects must not be pushed away from each other. In order to simulate an actual space capture environment, power to both the chaser and target robots was shut off. The target field robot moved at an initial velocity and then made contact with the end-effector of the manipulator. The chaser field robot moved with an initial velocity and was subsequently moved by the tension of the manipulator.

The insertion of a probe into a nozzle cone was considered as a potential method for the capture of a satellite. In order to successfully insert the manipulator into the target, a cylinder end-effector probe was employed to fulfill the task.

Figure 10 shows the initial status of the manipulator arm. Table II shows the selected values of inertia, damping, and stiffness matrices on the end-effector. The initial position and attitude of the base and target for the contact phase were:

$$X_{\mathrm{b}} = [0.2, 0.2, 0, 0^{\circ}, 0^{\circ}, 0^{\circ}] \tag{31}$$

and

$$X_{\mathrm{t1}} = [0.19, 0.4237, -0.5477, -2.67^{\circ}, 3.58^{\circ}, -2.13^{\circ}]. \tag{32}$$

https://doi.org/10.1017/S0263574714000587 Published online by Cambridge University Press

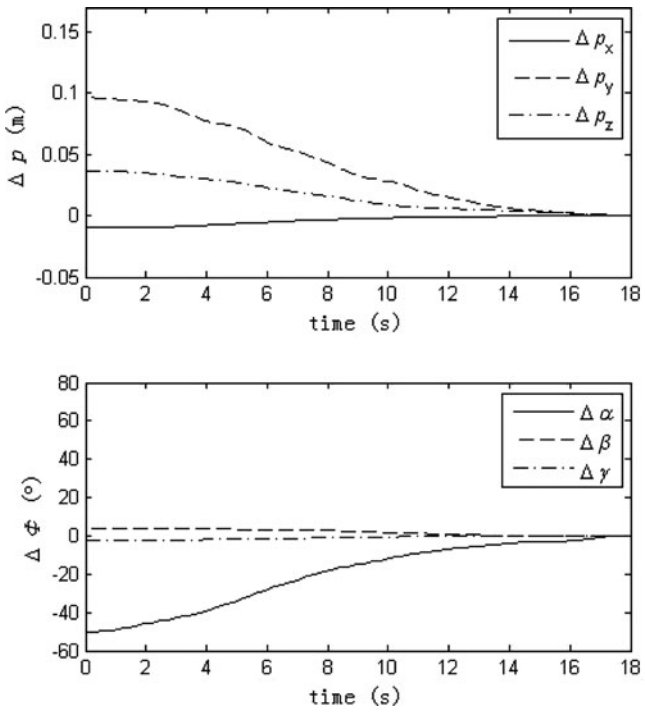

Fig. 8. The relative position and attitude between the end-effector and the handle.

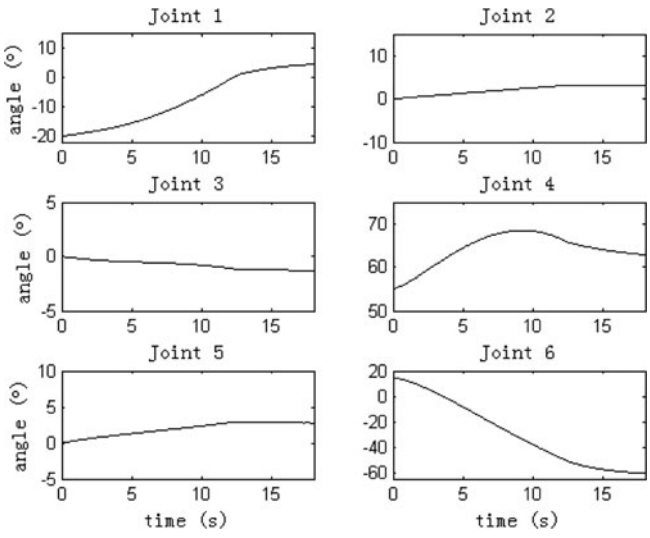

Fig. 9. The actual joint trajectory.

In this experiment, both the target and base were moving with an initial velocity of

$$\begin{cases} v_{b1} = v_{t1} = [10\ \text{mm/s}, 10\ \text{mm/s}, 0\ \text{mm/s}] \\ \omega_{b1} = \omega_{t1} = [0\ \text{deg/s}, 0\ \text{deg/s}, 0\ \text{deg/s}] \end{cases}. \tag{33}$$

In order to verify the effectiveness of the planning method for ensuring the protection of the manipulator arm, the experiment was divided into two parts. The first part used the original final position and attitude of the end-effector from the pre-contact phase as the initial condition. The second part added a deviation to the initial condition.

https://doi.org/10.1017/S0263574714000587 Published online by Cambridge University Press

Table II. Desired impedance parameters.

	x	*y*	*z*	Roll	Pitch	Yaw
M	100	100	100	500	500	500
D	200	200	200	500	500	500
K	100	100	100	500	500	500

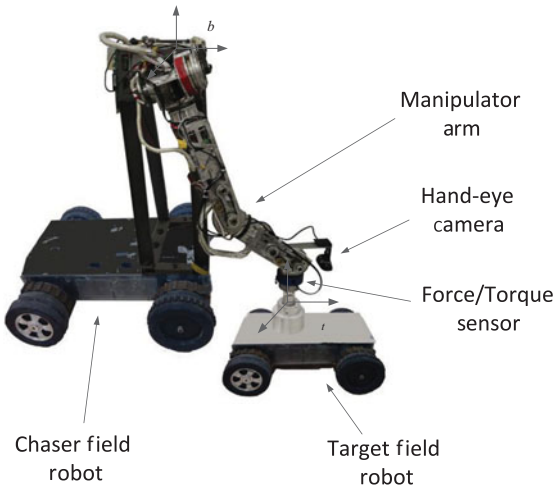

Fig. 10. Initial status of manipulator for force control.

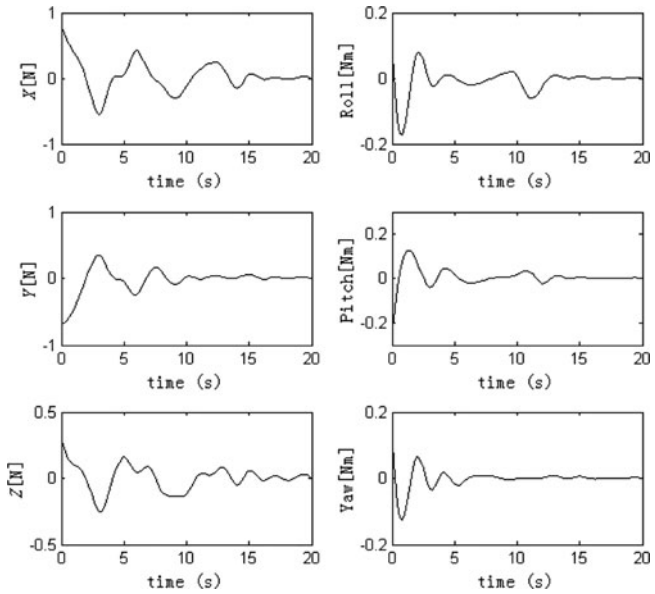

Fig. 11. Contact forces and torques without initial deviation.

6.4.1. Initial condition without deviation.

Here, the initial position and attitude of the end-effector were

$$X_{e1} = [0.19, 0.4237, -0.5477, -2.67^\circ, 3.58^\circ, -2.13^\circ]. \tag{34}$$

Figure 11 shows the contact forces and torques between the manipulator arm and the target. Figure 12 shows the velocities of the end-effector with respect to the base coordinate frame.

The contact forces were steadily suppressed and they gradually neared zero. The velocities of the manipulator arm gradually dampened out.

https://doi.org/10.1017/S0263574714000587 Published online by Cambridge University Press

Table III. Comparison of the two experiments.

	X(N)	Y(N)	Z(N)	Roll(Nm)	Pitch(Nm)	Yaw(Nm)	t(s)
Experiment 1	0.8	0.7	0.3	0.148	0.248	0.135	20
Experiment 2	1.2	1.2	0.31	0.248	0.298	0.137	29

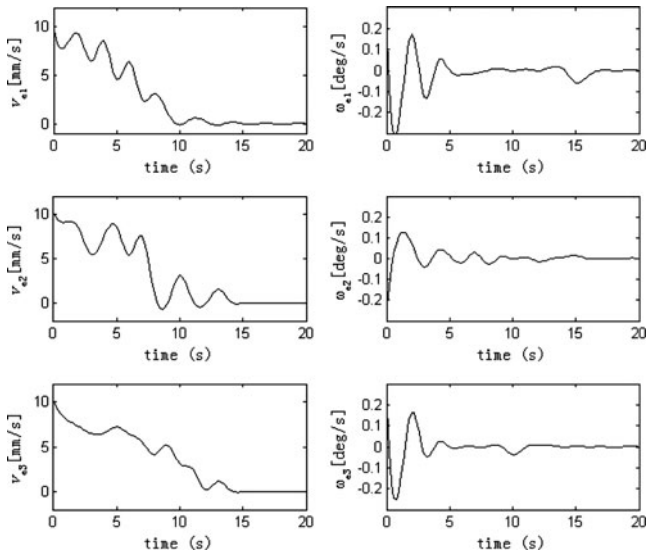

Fig. 12. Velocities of the end-effector without initial deviation.

6.4.2. Initial condition with deviation.

For comparison purposes, deviations, ΔX_{e1} were added to the initial attitude of the end-effector. These deviations were:

$$\begin{aligned} X_{e2} &= X_{e1} + \Delta X_{e1} \\ &= [0.19, 0.4237, -0.5477, -1.67^\circ, 4.58^\circ, -1.13^\circ]^{\cdot} \end{aligned} \tag{35}$$

Figure 13 shows the contact forces and torques between the manipulator arm and the target. Figure 14 shows the velocities of the end-effector with respect to the base coordinate frame. Table III shows a comparison between Figs. 11 and 13. The first line indicates the maximum value of each absolute value; t indicates the duration of the motion; *experiment 1* indicates the experiment for the initial condition without deviation; and *experiment 2* indicates the experiment for the initial condition with deviation.

Table III shows that for experiment 1, the maximum contact forces and torques were smaller and that the maximum time required to stabilize the motion of the system was less. This showed that an accurate capture strategy was essential for a target satellite and that the proposed visual servo method and the planning strategy were suitable for an accurate capture. Also, although there were initial deviations in experiment 2, the manipulator finally converged to stability, demonstrating the effectiveness of the force control method. Finally, less contact forces and contact duration time caused less damage to the manipulator arm, which enhanced the safety of the manipulator.

In summary, the control method enabled the end-effector of the manipulator to converge to the desired velocities and gradually suppressed the relative movement between the manipulator arm and the target. As a result, this method performed well in the protection of the manipulator arm.

7. Conclusion

This paper proposed a novel method to significantly increase protection for the manipulator arm while capturing a target satellite. This method makes the following contributions.

https://doi.org/10.1017/S0263574714000587 Published online by Cambridge University Press

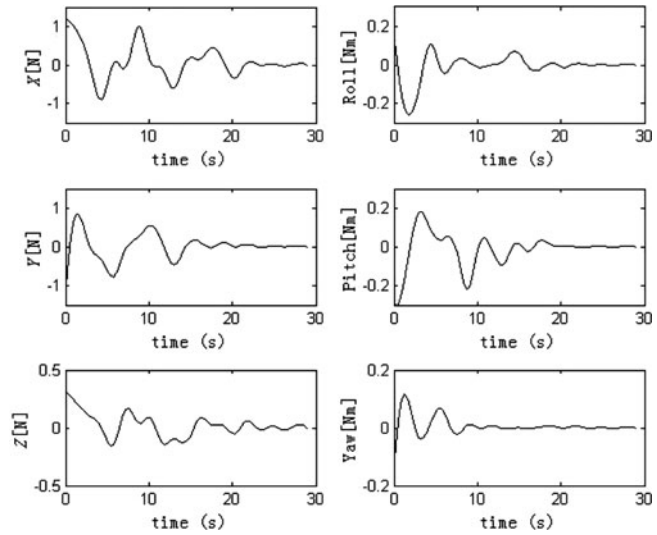

Fig. 13. Contact forces and torques with initial deviation.

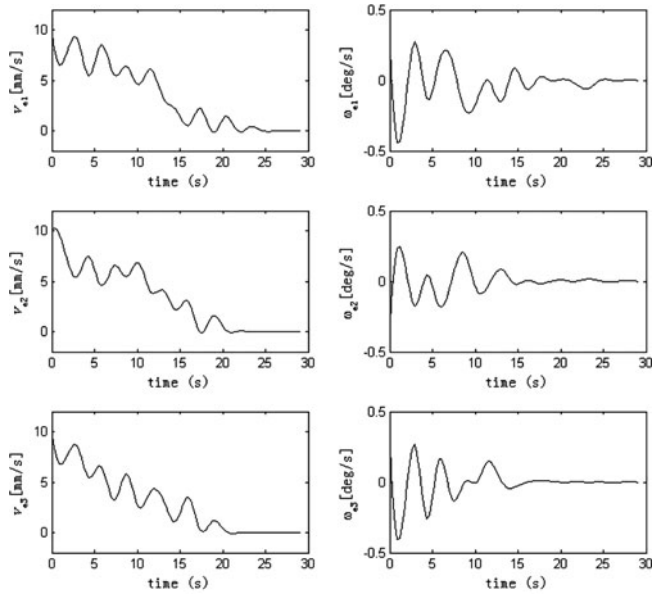

Fig. 14. Velocities of the end-effector with initial deviation.

1. The proposal of a high-precision, high-speed, visual servoing control method using a hand-eye camera.

2. The presentation of a motion planning method based on two cameras for the real-time capture of a target satellite.

3. The construction of a space robotic manipulator model that combines impedance control to ensure the safe capture of a target satellite.

4. The validation of the proposed method using an actual ground-based robotic system.

In order to deal with an actual space environment, the space robotic system must be able to cope with uncertainties such as space trash and indeterminate light. Flexible joints are needed to cope with these uncertainties. Further, the system must be able to recognize and capture non-cooperative targets in a space environment.

Finally, the algorithm in this current study focused on the accurate and safe capture of a target satellite. However, the overall system energy may not be minimal because the system energy was not

https://doi.org/10.1017/S0263574714000587 Published online by Cambridge University Press

considered in this study. Future research will focus on system optimization with regards to safety and energy consumption of the manipulator.

Acknowledgment

The authors wish to express their gratitude to the National High Technology Research of China (Grant 2011AA040202), the National Natural Science Foundation of China (Grants 60925014, 61320106012, 61375103, 61273348, and 61175077), and the Beijing Science Foundation (Grant 4122065) for their support of this work.

References

1. J. R. Wilson, "Satellite hopes ride on orbital express," *Aerospace Am.* **45**(2), 30–35 (2007).
2. J. Shoemaker and M. Wright, "Orbital Express Space Operations Architecture Program," *Proceedings of SPIE – The International Society for Optical Engineering*, Orlando, USA (Aug. 5–7, 2003) pp. 1–9.
3. M. Oda, "Space Robot Experiment on NASDAs ETS-VII Satellite," *Proceedings of IEEE International Conference on Robotics and Automation*, Detroit, USA (May 10–15, 1999) pp. 1390–1395.
4. G. Gibbs and S. Sachdev, "Canada and the International Space Station program: Overview and status," *Acta Astronaut.* **51**(1–9), 591–600 (2002).
5. H. Nagamatsu, T. Kubota and I. Nakatani, "Capture Strategy for Retrieval of a Tumbling Satellite by a Space Robotic Manipulator," *IEEE International Conference on Robotics and Automation*, Minneapolis, USA (Apr. 22–28, 1996) pp. 70–75.
6. W. Xu, B. Liang, C. Li and Y. S. Xu, "Autonomous rendezvous and robotic capturing of noncooperative target in space," *Robotica* **28**(5), 705–718 (2010).
7. W. F. Xu, B. Liang, C. Li, Y. Liu and Y. S. Xu, "Autonomous target capturing of free-floating space robot: Theory and experiments," *Robotica* **27**(3), 425–445 (2009).
8. T. Kobayashi and S. Tsuda, "Control of Space Robot for Moving Target Capturing," *International Multi-Conference of Engineers and Computer Scientists*, Hong Kong, P. R. China (Mar. 17–19, 2010) pp. 946–950.
9. Y. L. Gu and Y. Xu, "A Normal Form Augmentation Approach to Adaptive Control of Space Robot Systems," *IEEE International Conference on Robotics and Automation*, vol. 2, Atlanta, USA (May 2–6, 1993) pp. 731–737.
10. H. L. Wang and Y. C. Xie, "On the recursive adaptive control for free-floating space manipulators," *J. Intell. Robot. Syst.* **66**(4), 443–461 (2012).
11. D. N. Dimitrov and K. Yoshida, "Momentum Distribution in a Space Manipulator for Facilitating the Post-Impact Control," *IEEE/RSJ International Conference on Intelligent Robots and Systems*, Sendai, Japan (Sep. 28–Oct. 2, 2004) pp. 3333–3338.
12. W. Cheng, T. X. Liu and Y. Zhao, "Grasping strategy in space robot capturing floating target," *Chin. J. Aeronaut.* **23**(5), 591–598 (2010).
13. K. Yoshida *et al.*, "Dynamics, control, and impedance matching for robotic capture of a non-cooperative satellite," *RSJ Adv. Robot.* **18**(2), 175–198 (2004).
14. Z. Vafa and S. Dubowsky, "The kinematics and dynamics of space manipulators: The virtual manipulator approach," *Int. J. Robot. Res.* **9**(4), 3–21 (1990).
15. Y. Umetani and K. Yoshida, "Continuous path control of space manipulators mounted on OMV," *Acta Astronaut.* **15**(12), 981–986 (1987).
16. Y. Umetani and K. Yoshida, "Resolved motion rate control of space manipulators with generalized Jacobian matrix," *IEEE Trans. Robot. Automat.* **5**(3), 303–314 (1989).
17. X. C. Chen, Q. Huang, Z. G. Yu and Y. P. Lu, "Robust push recovery by whole-body dynamics control with extremal accelerations," *Robotica* 1–10 (2013).
18. G. Carbone, *Grasping in Robotics*, vol. 10 (Springer-Verlag, London, UK, 2013).
19. B. Weber and K. Kuhnlenz, "Visual Servoing Using Triangulation with an Omnidirectional Multi-Camera System," *Proceedings of the 11th International Conference on Control Automation Robotics & Vision*, Singapore (Dec. 7–10, 2010) pp. 1440–1445.
20. C. L. Chen and M. R. Lee, "Global Path Planning in Mobile Robot Using Omnidirectional Camera," *Proceedings of the International Conference on Consumer Electronics, Communication and Networks*, Xianning, P. R. China (Apr. 16–18, 2011) pp. 4986–4989.
21. Y. Wang, H. X. Lang and C. W. de Silva, "A hybrid visual servo controller for robust grasping by wheeled mobile robots," *IEEE/ASME Trans. Mechatronics* **15**(5), 757–769 (2010).
22. G. Allibert, "Predictive control for constrained image-based visual servoing," *IEEE Trans. Robot.* **26**(5), 933–939 (2010).
23. H. S. Wang, Y. H. Liu, W. D. Chen and Z. L. Wang, "A new approach to dynamic eye-in-hand visual tracking using nonlinear observers," *IEEE/ASME Trans. Mechatronics* **16**(2), 387–394, 2011.
24. Y. H. Liu, H. Wang and K. K. Lam, "Uncalibrated visual servoing of robots using a depth-independent image Jacobian matrix," *IEEE Trans. Robot.* **22**(4), 804–817 (2006).

25. S. A. Moosavian and E. Papadopoulos, "Free-flying robots in space: An overview of dynamics modeling, planning and control," *Robotica* **25**(5), 537–547 (2007).
26. W. F. Xu, B. Liang and Y. S. Xu, "Survey of modeling, planning and ground verification of space robotic systems," *Acta Astronautica* **68**(11), 1629–1649 (2011).
27. H. Nakanishi and K. Yoshida, "Impedance Control for Free-flying Space Robots – Basic Equations and Applications" *International Conference on Intelligent Robots and Systems*, Beijing, P. R. China (Oct. 9–15, 2006) pp. 3137–3142.
28. N. Hogan, "Impedance control: An approach to manipulation: part 1–3," *ASME J. Dynamic Syst. Meas. Control* **107**, 1–24 (1985).
29. K. Yoshida, "Experimental study on the dynamics and control of a space robot with the Experimental Free-Floating Robot Satellite (EFFORTS) simulators," *Adv. Robot.* **9**(6), 583–602 (1995).
30. C. R. Carignan and D. L. Akin, "The reaction stabilization of on-orbit robots," *IEEE Control Syst. Mag.* **20**(6), 19–23 (2000).
31. H. Sawada, K. Ui, M. Mori, "Micro-gravity experiment of a space robotic arm using parabolic flight," *Adv. Robot.* **18**(3), 247–267 (2004).
32. H. Ueno, Y. Wakabayashi, Y. Ohkami, S. Matunaga, R. Hayashi and T. Yoshida, "Ground testbed of a reconfigurable brachiating space robot," *Adv. Robot.* **14**(5), 355–358 (2000).
33. S. Dubowsky, W. Durfee, T. Corrigan, A. Kuklinski and U. Muller, "A Laboratory Test Bed for Space Robotics: The VES II," *International Conference on Intelligent Robots and Systems*, Munich, Germany (Sep. 12–16, 1994) pp. 1562–1569.

https://doi.org/10.1017/S0263574714000587 Published online by Cambridge University Press